

Article

Control of Grid-Connected and Standalone Microhydraulic Turbine Using a Six-Phase Induction Generator

Marius Ouédraogo, Amine Yazidi  and Franck Betin * 

Laboratory of Innovative Technologies (LTI, UR 3899), University of Picardie Jules Verne, 80000 Amiens, France; marius.ouedraogo@u-picardie.fr (M.O.)

* Correspondence: franck.betin@u-picardie.fr

Abstract: Microhydraulic turbines offer a promising solution for decentralized energy production, suitable for both grid-connected and standalone applications, due to their compactness and high efficiency. This paper introduces a control approach for such systems employing microhydraulic turbines as distributed generators (DGs), utilizing six-phase induction generators for electricity production. This study emphasizes control strategies for both grid-connected and standalone modes utilizing proportional-integral (PI) controllers. An integrated energy storage system based on Li-Ion battery technology is also implemented to store the excess energy and compensate for production deficits to meet demand. The results obtained using MATLAB/Simulink demonstrate efficient and reliable power management among production sources, the grid and the local load, highlighting the unique contribution of employing a six-phase induction generator with the energy storage system.

Keywords: six-phase induction generator; fault tolerant; microhydraulic turbine; wind turbine; energy storage; field-oriented control; grid-connected; standalone; bidirectional DC converter

1. Introduction

The increasing demand for electricity and challenges related to environmental sustainability have prompted the exploration of innovative energy alternatives using renewable energy sources [1] such as wind, solar, and hydroelectric power. In contrast to large-scale installations which operate using flowing water, these stand out for their cost-effectiveness, sustainability and environmental friendliness due to the absence of water reservoirs, making them more ecologic [2]. They emerge as a promising solution for clean and reliable electricity generation for grid-connected [3] and standalone [2] systems by harnessing the power of small watercourses.

Associating renewable energy with energy storage mechanisms is essential to address fluctuations in electricity demand, thereby ensuring a continuous and stable power supply for grid-connected systems [4]. It is also of particular importance for standalone applications, distant from the utility grid, reducing their dependence on conventional and costly energy sources with a reliable and sustainable supply.

The challenging conditions and difficult accessibility in which microhydraulic power plants operate can increase maintenance costs. Therefore, the robustness, reliability and efficiency of the generator used are crucial for ensuring reliable microhydraulic power generation in harsh and remote off-grid areas. In this context, the most suitable type of generator for microhydraulic applications is the induction machine, also known as an induction generator, which is well suited for such environments [5,6]. Additionally, the sustainability challenges of micro hydro power plants, as highlighted in the research, emphasize the importance of proper design, construction, operation, and maintenance of the generators to guarantee their efficiency and long-term viability [7]. In [8], the use of regulated electrical machines, such as induction dual-power machines, in small hydropower plants underscores their relevance and potential for addressing the maintenance and



Citation: Ouédraogo, M.; Yazidi, A.; Betin, F. Control of Grid-Connected and Standalone Microhydraulic Turbine Using a Six-Phase Induction Generator. *Energies* **2024**, *17*, 3581. <https://doi.org/10.3390/en17143581>

Academic Editor: Oscar Barambones

Received: 27 May 2024

Revised: 6 July 2024

Accepted: 17 July 2024

Published: 21 July 2024



Copyright: © 2024 by the authors. Licensee MDPI, Basel, Switzerland. This article is an open access article distributed under the terms and conditions of the Creative Commons Attribution (CC BY) license (<https://creativecommons.org/licenses/by/4.0/>).

robustness concerns in microhydraulic power generation. In the case of construction, using the classical three-phase induction machine is not electrical-fault-tolerant. One of the solutions consists of using a real multiphase machine associated with a corresponding converter [9].

Research studies have explored various configurations, including machines with four [10], five [11,12], six [13,14], seven [15], nine [16], and eleven phases [17]. Among these, machines with a number of phases that are multiples of three, such as the six-phase machine, have garnered particular interest. This is because they can be constructed from a conventional three-phase structure through simple rewinding [18], allowing them to leverage existing three-phase converters in the market.

Six-phase machines can be configured with either a single neutral point or two neutral points. In the case of a fault on one phase, the single neutral point configuration isolates only the faulty phase, whereas the two neutral points configuration deactivates the entire star of the affected phase. Six-phase machines are categorized into two types based on their phase displacement: symmetric [19] and asymmetric [20]. In the asymmetric configuration, where there is a 30° phase displacement between two phase groups, the torque ripple is lower compared to the symmetric configuration, which has a 60° phase displacement between phase groups.

Using a six-phase induction generator (6PIG) offers several advantages, including high-power handling capability by dividing the required power between phases, reduced torque pulsations, reduced stator copper losses, reduced rotor harmonic currents, and improved reliability [21]. This type of machine is suitable for medium- to high-power electric drive applications (20 KW–8 MW) and wind energy conversion systems [22]. In addition to the aforementioned advantages, another one is that in case of failure in one to three phases, the production still continues but the power is reduced and ripples appear. These ripples can be responsible for the destruction of the structure of the generator. To extract maximum power and to handle ripples in case of fault, several control strategies have been studied in the literature, such as Indirect Rotor Flux Oriented Controller (IRFOC) [23,24], Fuzzy Logic Controller (FLC) [25] and Variable Structure Controller (VSC) [26,27]. The control is performed using the generator side converter of the back-to-back converter system used to interface between the generator and the grid and the local load.

The microhydraulic system is a form of distributed generation (DG) [28] that is connected to the grid through a voltage source inverter (VSI). Voltage source inverters are commonly utilized as a power electronics interface to integrate renewable-energy-based distributed generation systems with the grid and microgrids [29]. VSIs are employed to convert DC power into AC power for supply to the grid [30] or the local load. With DG, VSI can operate in either the grid-connected mode or in the standalone mode, making them a reliable source of electrical power [31].

In grid-tied operation, DG delivers power to the utility and the local load. The objective of grid-connected renewable energy sources converters is to process power and inject sinusoidal currents into the grid. This system, which directly supplies power to the grid, is gaining popularity due to cost reductions [32]. To inject energy into the grid, the total harmonic distortion (THD) of the output current is limited to less than 5%, as defined by the IEEE standard 1547, to comply with the grid code and enhance the quality of electricity circulating in the electrical system [33,34]. Filters have been studied and designed to improve energy quality before grid injection, such as L, LC and LCL filters, which have been extensively researched. According to [35], these filters must effectively attenuate switching frequency harmonics while maintaining low impedance for the fundamental component. The comparison indicates that while the output voltage waveform remains consistent across filters, the LCL filter excels in distortion reduction and harmonic attenuation compared to L and LC filters. However, it introduces resonance and ripple issues [35], necessitating techniques like PI regulators based on dq models [36], active and passive damping methods [37] and passivity-based control [38,39] to ensure system stability and reduce independence between the filter and the grid impedance. Some studies have been

Section 2 will focus on the modeling and control of the six-phase induction generator. Grid-connected and standalone mode control schemes will be studied in Sections 3 and 4, respectively. Section 5 will examine the storage system as a whole. Lastly, Section 6 will be dedicated to the results and discussions, followed by the conclusion in Section 7.

2. Modeling and Control of a Six-Phase Induction Generator

2.1. Modeling

The squirrel cage six-phase induction generator (SC6PIG) is made up of a stator composed of six identical windings electrically phase shifted by 60° and a rotor composed of a metal bar and a short-circuit ring. The Figure 2 represents the stator of the SC6PIG.

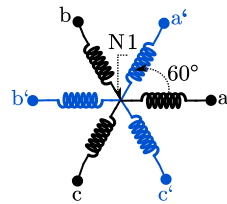


Figure 2. Six-phase stator windings.

Based on the main equations of voltage, torque, and rotor speed in the natural reference frame (aa'bb'cc') [42], the studied model corresponds to a simplified version of the equivalent interne circuit model [13,14,43]. The stator and rotor are represented by resistances, self-inductances, and mutual inductances. The equations for stator and rotor voltages are expressed as follows:

$$[V_{s6}] = [R_{s6}][I_{s6}] + \frac{d}{dt}[\phi_s] = [R_{s6}][I_{s6}] + [L_s] \frac{d}{dt}[I_{s6}] + [emf_s] \quad (1)$$

$$[V_{r6}] = [R_{r6}][I_{r6}] + \frac{d}{dt}[\phi_r] = [R_{r6}][I_{r6}] + [L_r] \frac{d}{dt}[I_{r6}] + [emf_r] \quad (2)$$

$$[\phi_s] = [L_{sr}] \times [I_{r6}] + [L_s][I_{s6}] \quad (3)$$

$$[\phi_r] = [L_{sr}]^T [I_{s6}] + [L_r][I_{r6}] \quad (4)$$

The stator and rotor voltages, currents, fluxes and resistances for the six stator and rotor windings are provided as follows:

$$\begin{aligned} [V_{s6}] &= [V_{sa} V_{sb} V_{sc} V_{sd} V_{se} V_{sf}]^T \\ [V_{r6}] &= [V_{ra} V_{rb} V_{rc} V_{rd} V_{re} V_{rf}]^T \\ [\phi_{s6}] &= [\phi_{sa} \phi_{sb} \phi_{sc} \phi_{sd} \phi_{se} \phi_{sf}]^T \\ [\phi_{r6}] &= [\phi_{ra} \phi_{rb} \phi_{rc} \phi_{rd} \phi_{re} \phi_{rf}]^T \\ [I_{s6}] &= [I_{sa} I_{sb} I_{sc} I_{sd} I_{se} I_{sf}]^T \\ [I_{r6}] &= [I_{ra} I_{rb} I_{rc} I_{rd} I_{re} I_{rf}]^T \\ [R_{s6}] &= \text{diag}_6(R_s) \\ [R_{r6}] &= \text{diag}_6(R_r) \end{aligned}$$

The electromagnetic torque equation, depending on the stator and rotor currents, is given by:

$$T_e = p [I_{s6}]^T \frac{\partial [L_{sr}]}{\partial \theta_r} [I_{r6}] \quad (5)$$

The relationship between the torque and the rotor speed is given by:

$$J \frac{d\Omega_r}{dt} + f\Omega_r = T_e + T_L \quad (6)$$

The simplified equation in the dq reference frame for the control is given by:

$$\begin{bmatrix} V_{sd} \\ V_{sq} \end{bmatrix} = \begin{bmatrix} R_s & 0 \\ 0 & R_s \end{bmatrix} \begin{bmatrix} I_{sd} \\ I_{sq} \end{bmatrix} + \begin{bmatrix} \frac{d\phi_{sd}}{dt} \\ \frac{d\phi_{sq}}{dt} \end{bmatrix} + \begin{bmatrix} 0 & -\omega_s \\ \omega_s & 0 \end{bmatrix} \begin{bmatrix} \phi_{sd} \\ \phi_{sq} \end{bmatrix} \quad (11)$$

With

$$\begin{bmatrix} \phi_{sd} \\ \phi_{sq} \end{bmatrix} = \begin{bmatrix} L_s & 0 \\ 0 & L_s \end{bmatrix} \begin{bmatrix} I_{sd} \\ I_{sq} \end{bmatrix} + \begin{bmatrix} M & 0 \\ 0 & M \end{bmatrix} \begin{bmatrix} I_{rd} \\ I_{srq} \end{bmatrix} \quad (12)$$

The expression of electromagnetic torque in the dq rotating reference frame is as follows:

$$T_e = pM(\phi_{rd}I_{sd} - \phi_{rq}I_{sd}) \quad (13)$$

The IRFOC method is realized by making the rotor flux follow only the d axis by turning the dq reference to cancel the q axis.

$$\begin{cases} \phi_{rd} = \phi_r \\ \phi_{rq} = 0 \end{cases} \quad (14)$$

The implementation requires the estimation or computation of θ_s from the rotor speed measure Ω and the pulsation of the slip ω_{sl} [45].

$$\theta_s = \int (\omega_r + \omega_{sl}) dt \quad (15)$$

To ensure decoupling, we need to set up stator currents' I_{sd} and I_{sq} regulation loops.

$$\begin{cases} V_{sd} = \sigma L_s \frac{di_{sd}}{dt} + \left(R_s + \frac{M^2 R_r}{L_r^2} \right) i_{sd} - \omega_s \sigma L_s i_{sq} + \frac{M R_r}{L_r^2} \phi_{rd} \\ V_{sq} = \sigma L_s \frac{di_{sq}}{dt} + \left(R_s + \frac{M^2 R_r}{L_r^2} \right) i_{sq} + \omega_s \sigma L_s i_{sd} + \frac{M}{L_r} p \Omega \phi_r \end{cases} \quad (16)$$

With the coefficient of dispersion $\sigma = 1 - \frac{M^2}{L_s L_r}$.

For the decoupled system, two new inputs (V_{sd1} , V_{sq1}) will be injected into the control [46].

$$\begin{cases} V_{sd1} = V_{sd} + fem_{sd} \\ V_{sq1} = V_{sq} + fem_{sq} \end{cases} \quad (17)$$

The compensation terms fem_{sd} and fem_{sq} are used in the news control with opposites sign to delete the coupling.

$$\begin{cases} fem_{sd} = \omega_s \sigma L_s i_{sq} + \frac{M R_r}{L_r^2} \phi_{rd} \\ fem_{sq} = -\omega_s \sigma L_s i_{sd} - \frac{M}{L_r} p \Omega \phi_r \end{cases} \quad (18)$$

The transfer function between the input and the output is finally given by:

$$\begin{cases} i_{sd} = \frac{L_r^2}{R_s L_r^2 + R_r M^2 + \sigma L_s L_r^2 s} V_{sd1} \\ i_{sq} = \frac{L_r^2}{R_s L_r^2 + R_r M^2 + \sigma L_s L_r^2 s} V_{sq1} \end{cases} \quad (19)$$

By analogy to a second-order system, we can deduce the proportional integral (PI) regulator parameters:

$$\begin{cases} K_i = \omega_n^2 \times \sigma L_s \\ K_p = K_i \left(\frac{2\xi}{\omega_n} - \frac{M^2}{L_r T_r K_i} - \frac{R_s}{K_i} \right) \end{cases} \quad (20)$$

3. Grid-Connected Control Scheme

3.1. Voltage Source Inverter for Grid-Connected and Standalone Mode

VSI is essential for both grid-connected and standalone system. It permits the extraction and the injection of the power to the grid and/or the local load.

In the grid-connected mode, the voltage and frequency are determined by the grid, and the VSI operates as a current-controlled inverter. This means that within their nested control loops systems, the inner loops manage current, while the outer loops handle active and reactive power control or DC link voltage control [29].

In the standalone mode, the VSI is in charge for adjusting the voltage and frequency for local load [47]. Because of the lack of the utility grid, the output voltage has to be controlled in terms of magnitude and frequency. This means that, although the inner control loops in their nested control loop system are current controllers, similar to grid-connected VSIs, the outer loops are the output AC voltage controllers [29].

Several methods are studied for controlling the VSI for the both modes. In this paper, the PI controller based on the dq reference frame is used. In this method, PI controllers are used as regulators ensuring a zero steady-state [29].

3.2. DC Link Control

The DC link is a component of the energy conversion system that allows to maintain the constant continuous voltage to supply others electric components within the conversion chain. The DC bus control is essential in energy storage system and grid energy injection applications since it permits to guarantee the supply stability and energy conversion efficiency and also realize the active power flux transfer drawn from the generator to the grid. The equation of the DC link voltage is given by:

$$\frac{dV_{dc}}{dt} = \frac{1}{C_{dc}} \left(I_{dc} - \frac{V_{dc}}{R_{dc}} \right) \quad (21)$$

V_{dc} , C_{dc} and R_{dc} are, respectively the DC link voltage, capacitor and resistor.

For the control, we use voltage regulator such as PI that adjust the control of supply converters for compensate load variation or voltage in generator side at the converter output. The transfer function of the DC bus is:

$$G_{dc}(s) = \frac{1}{sC_{dc}} \quad (22)$$

The closed loop transfer function is:

$$T(s) = \frac{k_p s + k_i}{C_{dc} s^2 + k_p s + k_i} \quad (23)$$

The regulator parameters are determined by analogy between the DC bus and the quadratic transfer function. PI regulator parameters are found by these equations:

$$\begin{cases} k_i = \omega_n^2 C_{dc} \\ k_p = 2\xi\omega_n C_{dc} \end{cases} \quad (24)$$

3.3. Grid Currents Control

Some scientific studies have analyzed systems connected to single-phase [32,48] and three-phase electrical grids [49,50]. Single-phase grids, commonly used in residential and small business applications are studied for their energy efficiency, load management and integration of renewable energy sources. Three-phase grids favored in industrial and commercial contexts are the focus of research on optimizing energy distribution, reducing electrical losses, and improving grid stability. These studies highlight the specific challenges

and opportunities for each type of grid in the context of energy transition and sustainable development. Our study will focus on the connection to three-phase electrical grids.

The third-order filter chosen for our study provides better harmonic attenuation. This improves the quality of the energy transiting through the utility grid to comply with current standards. The figure below depicts a schematic of one phase of the LCL filter.

Based on Figure 4, the Kirchhoff's Voltage Law permits to write the expressions in inverter and grid side for one phase that is given by:

$$\begin{cases} L_1 \frac{dI_1(t)}{dt} + R_1 I_1(t) = V_c - V_{inv} \\ L_2 \frac{dI_2(t)}{dt} + R_2 I_2(t) = V_{grid} - V_c \end{cases} \quad (25)$$

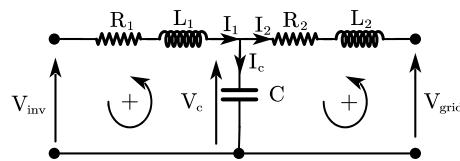


Figure 4. Single phase of LCL filter.

The Node rule permits to write the relationship between currents:

$$C \frac{dV_c(t)}{dt} = I_1(t) - I_2(t) \quad (26)$$

By applying park transformation denoted T,

$$T = \sqrt{\frac{2}{3}} \begin{bmatrix} \cos \theta & \cos(\theta - \frac{2\pi}{3}) & \cos(\theta - \frac{4\pi}{3}) \\ -\sin \theta & -\sin(\theta - \frac{2\pi}{3}) & -\sin(\theta - \frac{4\pi}{3}) \\ \frac{1}{\sqrt{2}} & \frac{1}{\sqrt{2}} & \frac{1}{\sqrt{2}} \end{bmatrix} \quad (27)$$

the LCL filter model in the dq rotating reference frame is as follows:

$$\begin{cases} \frac{dI_{1d}}{dt} = \omega I_{1q} - \frac{R_1}{L_1} I_{1d} + \frac{1}{L_1} V_{invd} - \frac{1}{L_1} V_{cd} \\ \frac{dI_{1q}}{dt} = -\omega I_{1d} - \frac{R_1}{L_1} I_{1q} + \frac{1}{L_1} V_{invq} - \frac{1}{L_1} V_{cq} \\ \frac{dI_{2d}}{dt} = \omega I_{2q} - \frac{R_2}{L_2} I_{2d} - \frac{1}{L_2} V_{cd} + \frac{1}{L_2} V_{gridd} \\ \frac{dI_{2q}}{dt} = -\omega I_{2d} - \frac{R_2}{L_2} I_{2q} - \frac{1}{L_2} V_{cq} + \frac{1}{L_2} V_{gridq} \\ \frac{dV_{cd}}{dt} = \omega V_{cq} + \frac{1}{C} I_{1d} - \frac{1}{C} I_{2d} \\ \frac{dV_{cq}}{dt} = -\omega V_{cd} + \frac{1}{C} I_{2d} - \frac{1}{C} I_{1d} \end{cases} \quad (28)$$

The dq model obtained allows to set up the currents control with PI regulator. In high frequency, the capacity is having like a wire and the voltage is closed to zero. By neglecting the capacity, we have:

$$\begin{cases} V_{gridd} = -V_{invd} - \frac{dI_{1d}}{dt} - R I_{1d} + L \omega I_{1q} \\ V_{gridq} = -V_{invq} - \frac{dI_{1q}}{dt} - R I_{1q} - L \omega I_{1d} \end{cases} \quad (29)$$

With $L = L_1 + L_2$, $R = R_1 + R_2$.

Assuming the above equations, we can write:

$$\begin{cases} V_{gridd_ref} = -\left(K_P + \frac{K_I}{s}\right) (I_{dref} - I_d) + L \omega I_{1q} + V_{gridd} \\ V_{gridq_ref} = -\left(K_P + \frac{K_I}{s}\right) (I_{qref} - I_q) - L \omega I_{1d} + V_{gridq} \end{cases} \quad (30)$$

With

$$\begin{cases} \left(K_P + \frac{K_I}{s}\right)(I_{dref} - I_d) = L \frac{dI_d}{dt} + RI_d \\ \left(K_P + \frac{K_I}{s}\right)(I_{qref} - I_q) = L \frac{dI_q}{dt} + RI_q \end{cases} \quad (31)$$

The equations in the dq rotating reference frame introduce cross-coupling between the d and q axes, which deteriorates the control system performance. For this grid-connected VSI, a decoupling technique in the d and q axes' currents' control loops is required. This technique helps to suppress the sensitivity to the load changes, enhances disturbance rejection capability, and improves the output current THD in the presence of non-linear loads [23].

3.4. Active and Reactive Power Control

With the dq rotating reference frame, V_{gridd} becomes constant and corresponds to the grid's rated voltage and V_{gridq} becomes zero. The active power is controlled by the d axis' current reference signal determined by the output of V_{dc} as follows [51]:

$$P_{dc*} = V_{dc} \times I_{dref} \quad (32)$$

The active power delivered to the grid is:

$$P_{grid*} = P_{dc*} + P_{inv} + P_f \quad (33)$$

where P_f is filter power absorbed by resistances and P_{inv} is the loss power owing to the condition and commutation. By neglecting the loss powers, we have:

$$P_{grid*} = P_{dc*} \quad (34)$$

Then, I_{dref*} is obtained by:

$$I_{dref*} = \frac{V_{dc} I_c}{V_{grid}} \quad (35)$$

The reactive power is controlled by setting the quadratic current reference I_{qref} to zero, because only active power must be injected to the grid. Thereby, we have to set up:

$$I_{qref} = 0 \quad (36)$$

The active and reactive power of the grid can be determined by:

$$\begin{cases} P = V_d I_d + V_q I_q \\ Q = V_q I_d - V_d I_q \end{cases} \quad (37)$$

3.5. Grid Synchronization

To connect a system to a three-phase electrical grid utility via an inverter, it is essential that the inverter output voltage be synchronized with that of the grid. This involves the frequency and the phase of the output voltage of the inverter corresponding to those of the grid. Several methods are used in the literature. The method used in this paper is a phase-locked loop (PLL), which generates an output signal that synchronizes the input signal in phase and frequency using regulation loop. The synchronization process is carried out in real time, which causes the loop to work constantly.

The control system in the grid-connected mode is shown in the following Figure 5.

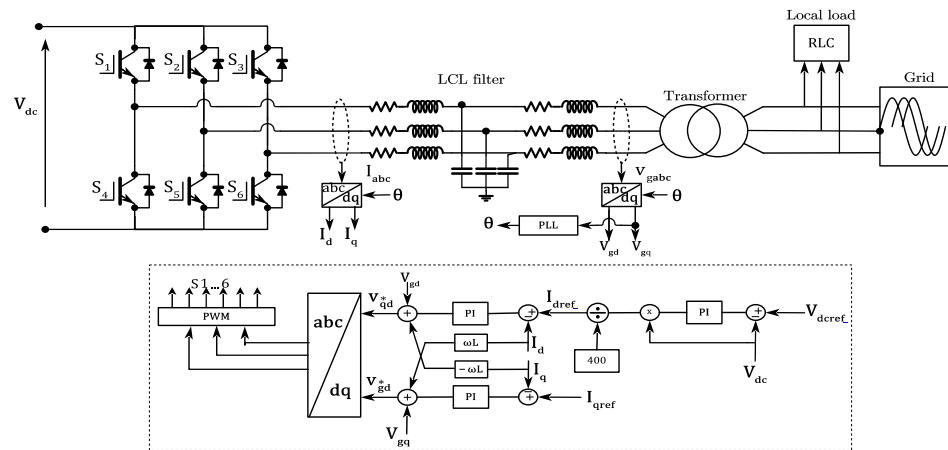


Figure 5. Grid-connected system control.

4. Control Scheme for Standalone Mode

Standalone systems have been extensively studied in the literature [29,52]. These systems, which operate independently of the main electrical grid, are particularly relevant in remote or rural areas where access to the grid is limited or nonexistent. Research on standalone systems focuses on several aspects to improve their efficiency, including optimization of renewable energy sources, energy storage management, energy efficiency and load management.

Based on the aforementioned Figure 4, the Kirchhoff’s Voltage Law and the Node rule allow us to write the following formula:

$$L \frac{dI(t)}{dt} + RI(t) = V_i - V_L \tag{38}$$

$$C \frac{dV_c(t)}{dt} = I_i - I_o \tag{39}$$

In applying Park transformation, the filter model in the dq rotating reference frame becomes:

$$L \frac{d}{dt} \begin{bmatrix} I_{Ld} \\ I_{Lq} \end{bmatrix} = \begin{bmatrix} -R & \omega L \\ -\omega L & R \end{bmatrix} \begin{bmatrix} I_{Ld} \\ I_{Lq} \end{bmatrix} + \begin{bmatrix} V_{id} - V_{cd} \\ V_{iq} - V_{cq} \end{bmatrix} \tag{40}$$

$$C \frac{d}{dt} \begin{bmatrix} V_{cd} \\ V_{cq} \end{bmatrix} = \begin{bmatrix} C\omega V_{cd} \\ -C\omega V_{cq} \end{bmatrix} + \begin{bmatrix} I_{Ld} - I_{od} \\ I_{Lq} - I_{oq} \end{bmatrix} \tag{41}$$

with Laplace transformation, we have:

$$\begin{bmatrix} I_{Ld} \\ I_{Lq} \end{bmatrix} = \frac{1}{LS + R} \left(\begin{bmatrix} V_{id} - V_{cd} \\ V_{iq} - V_{cq} \end{bmatrix} + \begin{bmatrix} \omega L I_{Lq} \\ \omega L I_{Ld} \end{bmatrix} \right) \tag{42}$$

$$\begin{bmatrix} V_{cd} \\ V_{cq} \end{bmatrix} = \frac{1}{CS} \left(\begin{bmatrix} C\omega V_{cd} \\ -C\omega V_{cq} \end{bmatrix} + \begin{bmatrix} I_{Ld} - I_{od} \\ I_{Lq} - I_{oq} \end{bmatrix} \right) \tag{43}$$

In grid-connected operation and in standalone VSI, cross-coupling exists in both current and voltage control loops. In [47], a damp resistor controller is used to dissipate excess power during fault or over generation. For improving the dynamic performance of the controller in this work, the cross couplings terms are nullified by the decoupled network with feed-forward signals V_{cd} and V_{cq} . The VSI must maintain an output voltage with low Total Harmonic Distortions (THD) for all types of loads. The THD level should comply with the IEEE standard 1547, which sets a limit of 5% [53].

Figure 6 illustrates the control system in standalone mode used in this paper.

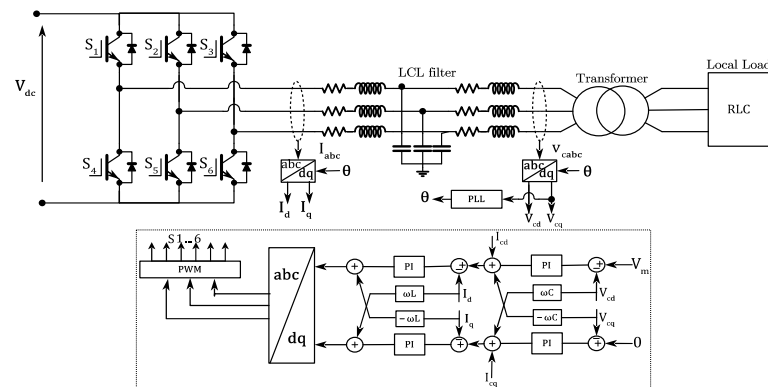


Figure 6. Standalone system control.

5. Energy Storage System

The energy storage system is essential for integrating renewable energies, addressing the intermittent and less predictable nature of sources. An energy storage system serves various purposes:

- (1) For isolated locations, it ensures autonomy by building up an energy reserve during periods of excess production and releasing it when production temporarily falls short or stops. It means that it ensures the balance of energy between the source and the local load [53].
- (2) For grid-connected systems, it maintains a real-time balance between production and consumption, improves the stability and reliability of the grid, and promotes a more efficient use of renewable energies, reducing dependence on fossil fuels and associated greenhouse gas emissions from electricity production using polluting energy sources.

Several storage technics are used in the literature, including a battery storage system, which store energy in the form of chemical energy and release it in the form of electrical energy by oxidation and reduction of their materials. The battery storage system is preferred over other storage technics or devices due to its performance and significantly higher energy density [53]. Assuming all the various types of battery storage system studied in the literature, lithium-ion technology is one of the best compromises in terms of energy density, energy efficiency (between 95% and 99%), duty life, low self-discharge, very low memory effect and high flexibility, as well as in terms of energy/power ratio.

Bidirectional DC/DC Converter Control

The growing demand for generating power from renewable energy sources has made energy storage and the integration of energy storage devices with the grid a significant challenge. A bidirectional DC-DC converter (BDC) provides the required bidirectional power flow for battery charging and discharging [54]. It is based on the power demand of the local load and the microturbine, employing a six-phase induction generator input. Bidirectional DC-DC converters are of two types: non-isolated and isolated topologies. The transformer-less, non-isolated topology is simple and has a reduced number of components with more efficiency than isolated BDC [55].

The BDC is constituted of IGBT (Q_i) in parallel with a diode D_i ($i = 1-2$), as shown in Figure 7.

When transistor Q_2 and diode D_1 are switched ON, the bidirectional converter (BDC) functions as a boost converter, supplying power to the local load in a discharging or injecting mode. Conversely, when transistor Q_1 and diode D_2 are switched ON, the BDC operates as a buck converter, injecting power into the battery during a charging or harvesting mode. This means that the BDC is used to increase the output voltage when there is high demand from the local load, while it functions in buck mode to protect the battery by providing optimal charging voltage [55].

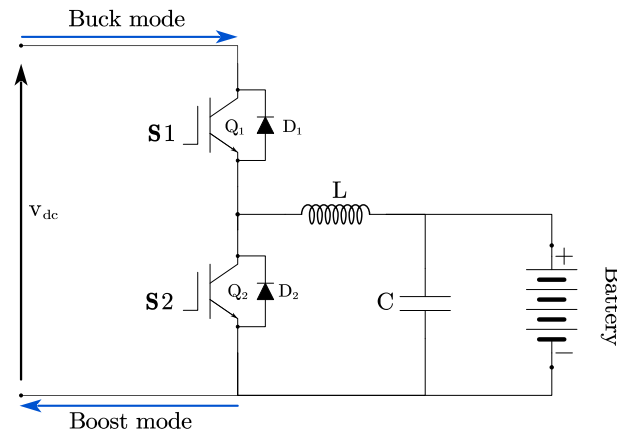


Figure 7. Bidirectional DC converter with the battery.

Several studies have focused on voltage and/or current regulation for BDCs. In these studies, a proportional-integral (PI) control strategy is employed to track the reference voltage or current of the bidirectional converter. An inner current loop is utilized to stabilize battery current against any system fluctuations in both grid-connected and standalone modes. In standalone mode, an outer voltage loop also regulates the DC link voltage, maintaining it at a constant value as a reference while managing charge/discharge currents to/from the battery bank based on the required local load power [56].

The DC link voltage V_{dc} is sensed and compared with a reference voltage V_{dcref} . The error signal is then processed with a PI controller to generate the reference of battery current I_{batref} . I_{batref} is compared with the sensed battery current I_{bat} and the resulting error is passed through the second PI controller. This generates the control modulation signal for pulse width modulation (PWM), as depicted in Figure 8. To ensure the modulation signal remains within the range of ± 1 , a saturation block is employed.

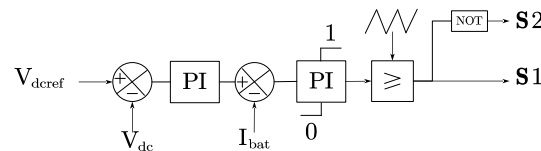


Figure 8. Bidirectional DC converter control.

6. Results and Interpretation

As the test bench does not include all the required elements, such as the storage system, only the experimental results from the six-phase induction generator side will be presented in this paper and compared to those from the simulation. Therefore, only the simulation results will be discussed in the remainder of this study. The experimental results will be addressed in another article, pending the receipt of the missing equipment.

Figure 9 depicts the currents of the six phases of the induction generator both in simulation (a) and experimentation (b) for several distinct levels of stator currents references.

Figure 10a,b represents, respectively, the direct and quadratic currents of the six-phase induction generator both in simulation and experimentation, while Figure 11a,b depicts the simulated and experimental electromagnetic power delivered by the induction generator.

Figures 9–11 show that the model of the six-phase induction generator associated with the control used for simulation is realistic since the experimental and simulation results are very close.

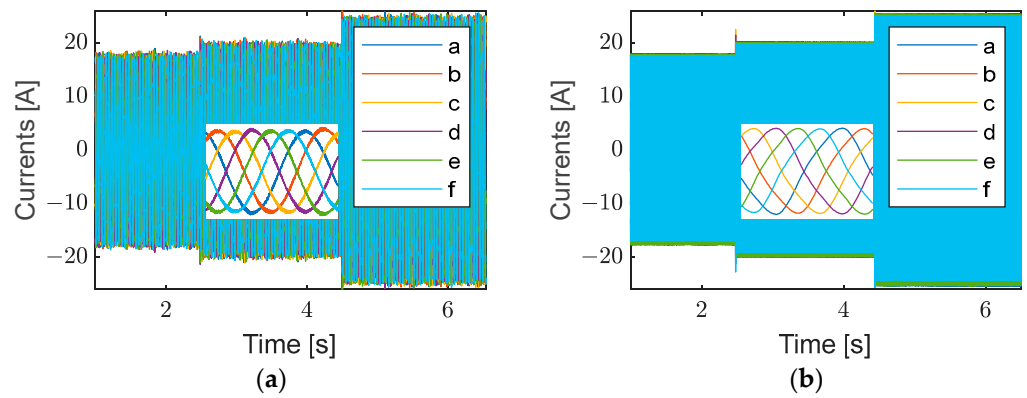


Figure 9. (a) Simulation result of the generator stator currents, (b) experimental result of the generator stator currents.

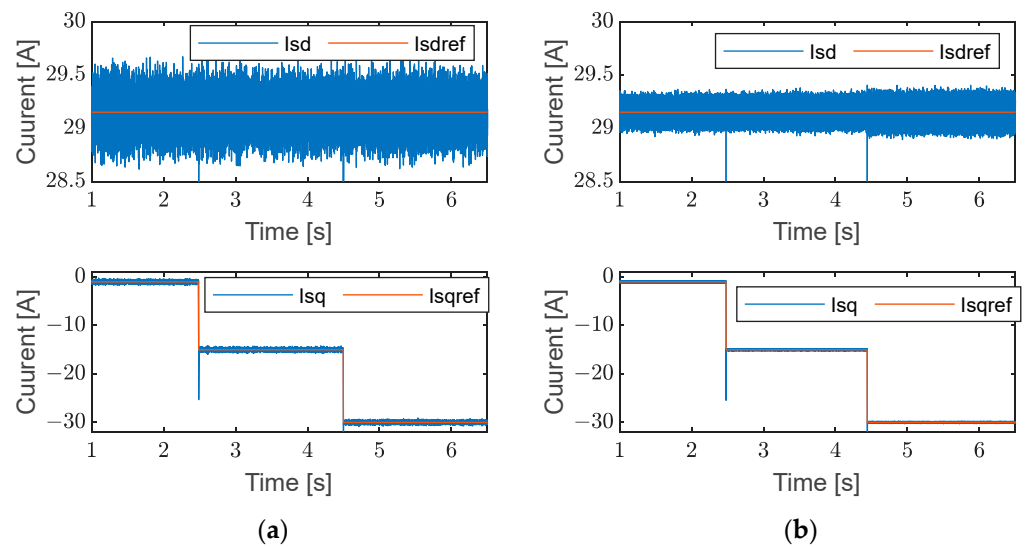


Figure 10. Direct and quadratic current: (a) simulation and (b) experimentation.

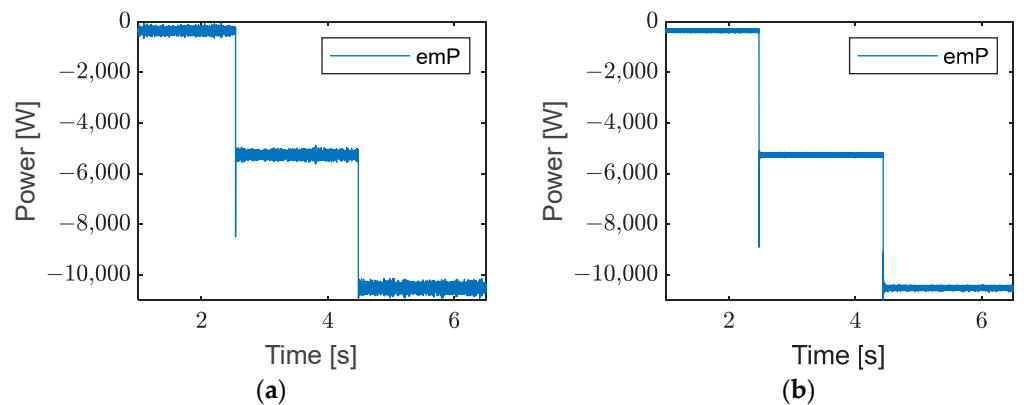


Figure 11. Electromagnetic power: (a) simulation and (b) experimentation.

6.1. Results in Grid-Connected Mode

6.1.1. Without Local Load

In this section, the grid-connected system operates without any load. The aim is to demonstrate the effectiveness and efficiency of managing flow transfers such as injection into the grid or storage in the battery, as shown by the results below.

In this scenario of Figure 12, from 0 to 2.5 s, only the battery supplies energy to the grid (magenta color). During this period, the generator flux is expected to reach its nominal

value. The generator is loaded at $-500 \text{ N}\cdot\text{m}$ at $t = 2.5 \text{ s}$ (green color), resulting in an increase in the power injected into the grid (blue color). The battery supply is interrupted at 3.5 s . At 5 s , the contribution of the generator, loaded at $-1000 \text{ N}\cdot\text{m}$, increases, and some of the generated energy is used to recharge the battery. Throughout the scenario, the reactive power of the grid (red color) is maintained at 0 .

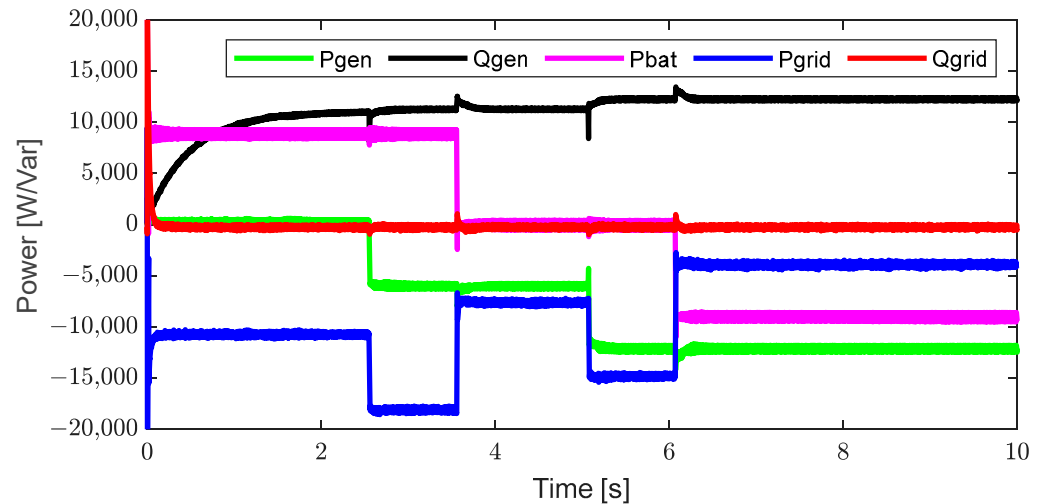


Figure 12. Active and reactive power of the generator, battery and the grid.

Figure 13 represents the currents on the inverter side (Figure 13a) and the grid side (Figure 13b). In this scenario, the magnitudes of the currents are nearly the same. The only point of difference is the quality of the currents. Those from the inverter contain harmonics due to the switching of the switches (semiconductors). Owing to the LCL filter, those from the grid are significantly cleaner and comply with grid standards. In Figure 14, it is noticeable that the total harmonic distortion (THD) of the grid current (Figure 14b) is significantly lower than 5%, which complies with the standards of the electrical grid. This is attributed to the LCL filter.

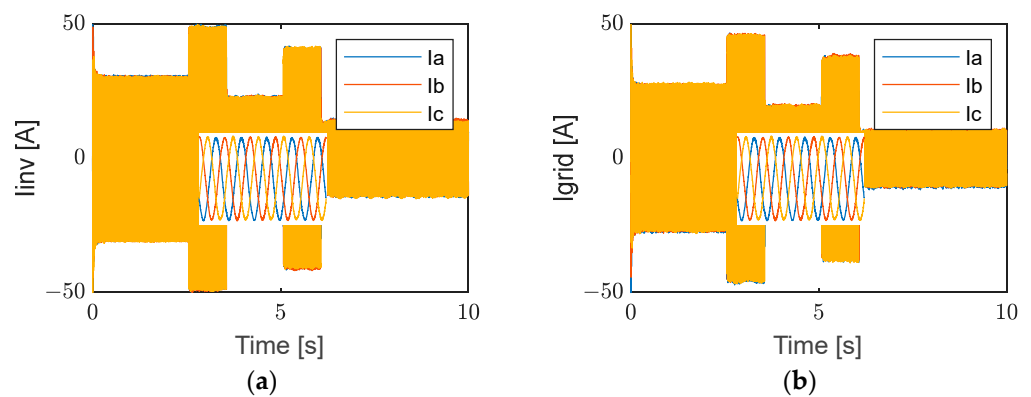


Figure 13. (a) Inverter currents. (b) Grid currents.

6.1.2. With Local Load

As in the previous section, the grid-connected system now supplies a local load. In this scenario, a 10 KW load is added (cyan color). Initially, between 0 and 2 s , no energy is supplied by the generator or the battery; so, all the energy required for the local load comes from the grid (indicated in blue). At $t = 2 \text{ s}$, the storage system (magenta color) begins to power the local load. By charging the generator (green color) at $t = 3 \text{ s}$, there is enough energy to supply the load, and the surplus is fed back into the grid. At 5 s , the battery supply is discontinued, and the generator supply is increased, with still sufficient energy for the local load and surplus fed back into the grid. One second later, grid injection is

stopped, and the surplus is used to charge the battery. Contrary to the scenario without the local load, where the reactive power (red color) of the grid is zero, here, it has a fixed value corresponding to the reactive power of the local load (yellow color) due to disturbances related to the LCL filter (Figure 15).

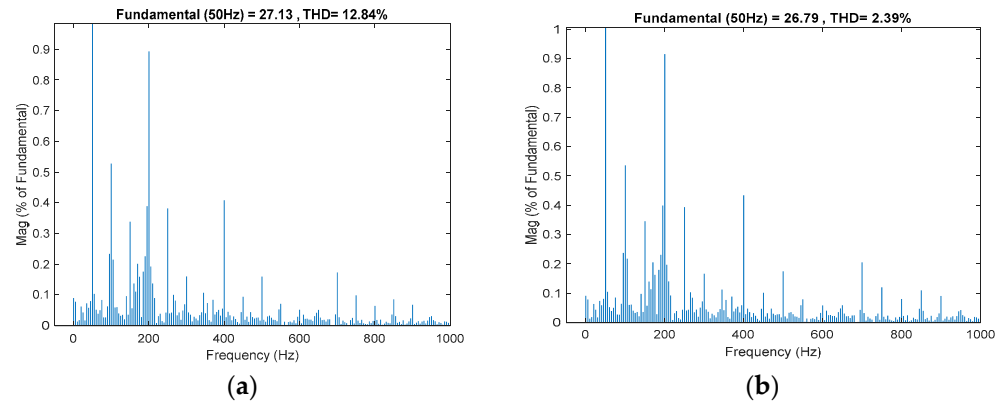


Figure 14. The harmonic distortion rate in grid-connected mode without load of (a) inverter currents and (b) grid currents.

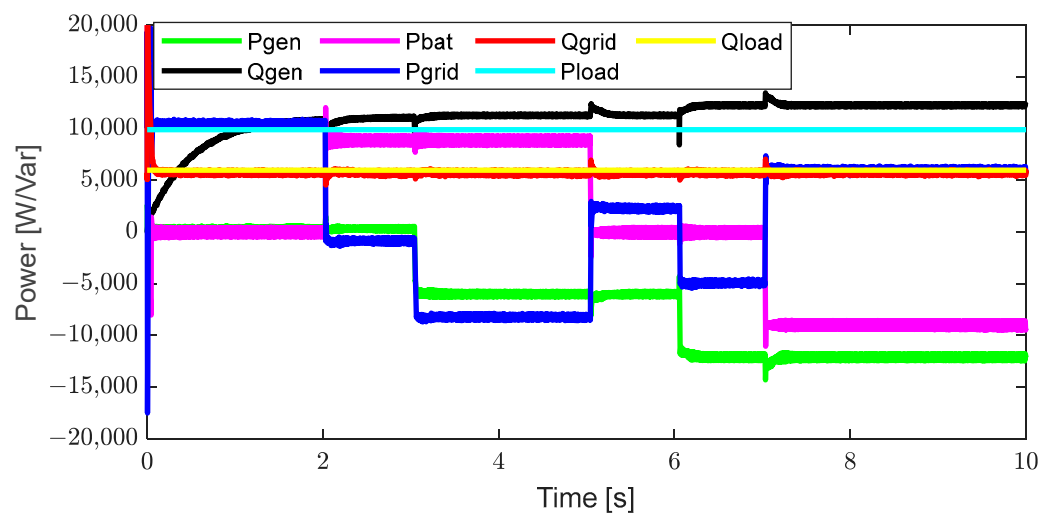


Figure 15. Active and reactive power of the generator, the battery, the grid and the local load.

Figure 16 represents the currents on the inverter side (Figure 16a) and the grid side (Figure 16b). In contrast to the previous scenario, the two currents are not identical due to the load, which can draw energy from sources such as the six-phase induction generator and the battery, or from the grid in case of production shortfall. It should be noted that in the event of abundant production, the surplus is injected into the grid or used to charge the battery. In Figure 17, despite the presence of the local load, the grid-side current has a total harmonic distortion (THD) of less than 5%.

Since the load remains constant throughout the simulation, the current also remains constant, as shown in Figure 18.

6.2. Standalone Mode Results

In this section, the system operates in standalone mode, meaning without a grid utility connection. Power sources such as the six-phase induction generator and battery directly and exclusively supply the local load. In an autonomous system, there is no grid; so, the voltage magnitude and frequency are generated by the inverter. In this scenario shown in Figure 19, if the generator output (green color) is lower than what the load requires (cyan color), the deficit is drawn from the battery (magenta color). Similarly, if it exceeds the

load’s requirements, the surplus is used to charge the battery. Initially set at 7 kW, the local load is increased to 10 kW at $t = 5$ s.

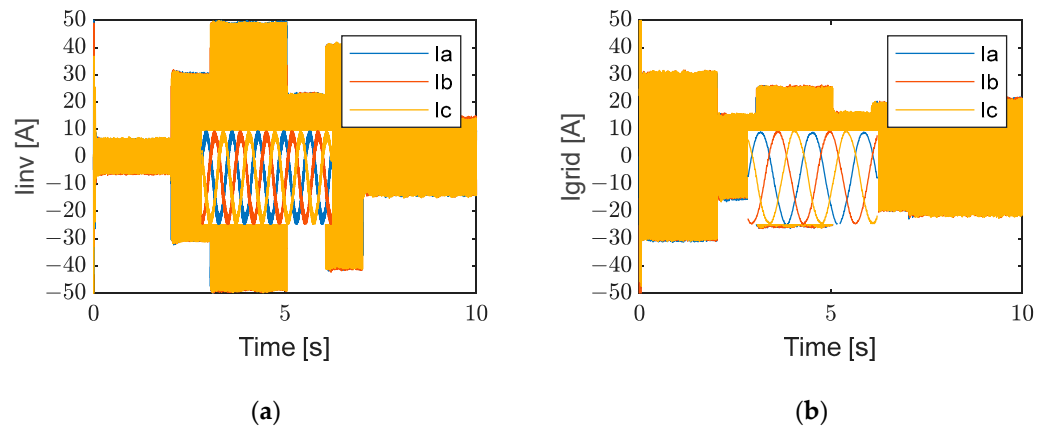


Figure 16. (a) Inverter currents. (b) Grid-side currents.

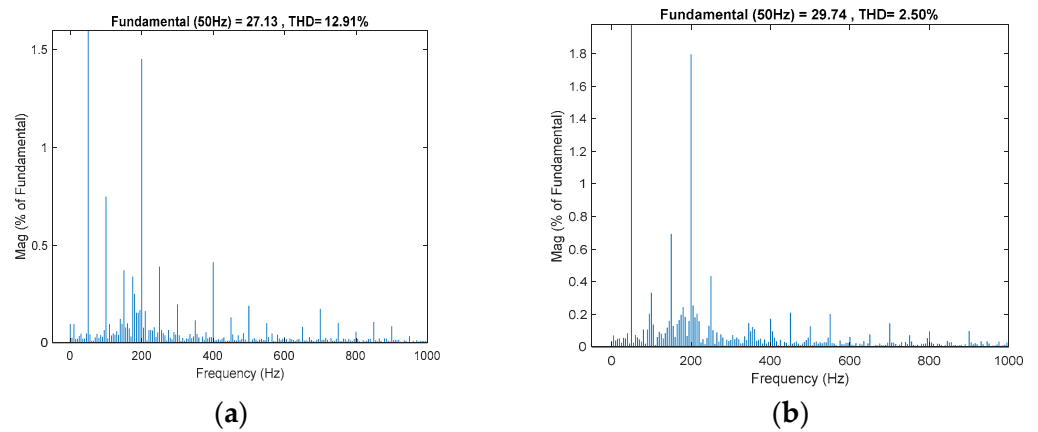


Figure 17. The harmonic distortion rate in grid-connected mode with load of (a) inverter currents and (b) grid currents.

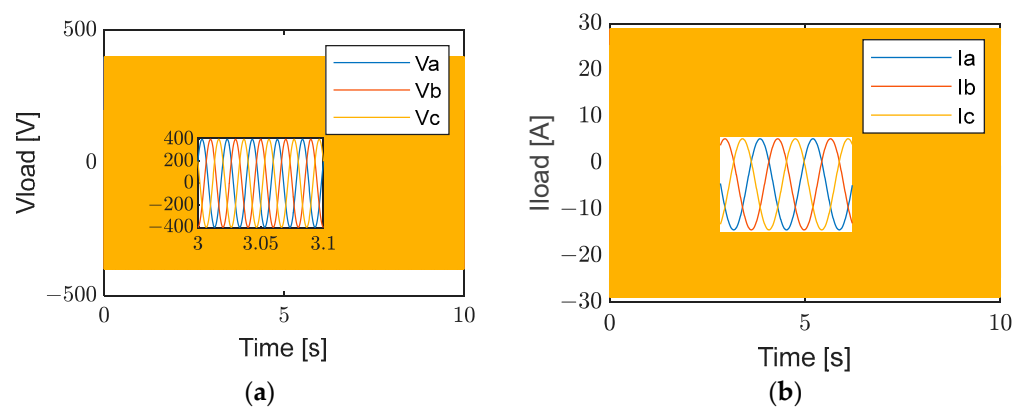


Figure 18. (a) Load voltage. (b) Load currents.

Despite the absence of the grid utility, it can be noted that the voltage of the local load is perfectly controlled at a peak magnitude of 400 V (as shown in Figure 20a). As the local load is not constant, the current follows the trends of its evolution shown in Figure 20b.

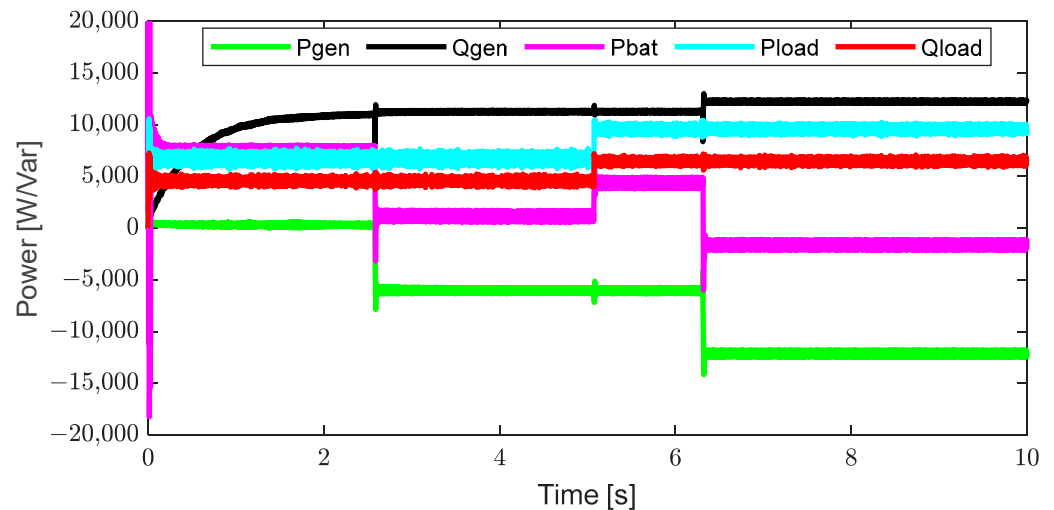


Figure 19. Active and reactive power of the generator, the battery and the local load.

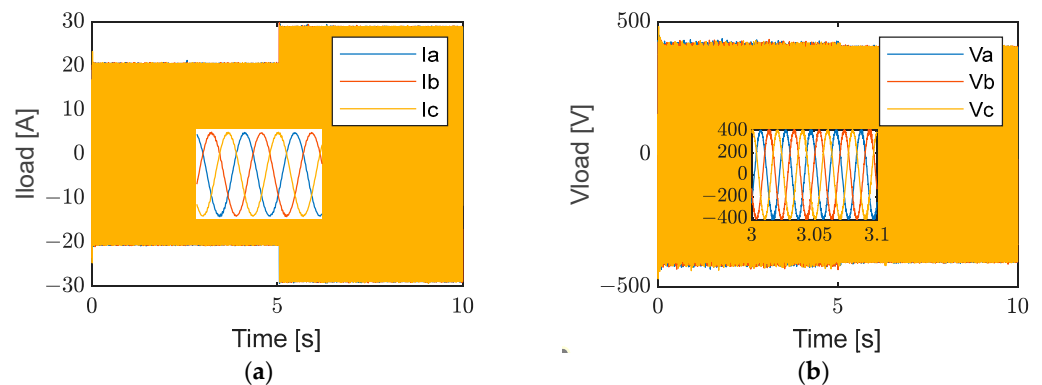


Figure 20. (a) Local load voltage and (b) the local load current.

7. Conclusions

In conclusion, this study demonstrates the feasibility and effectiveness of utilizing microhydraulic turbines as distributed generators coupled with six-phase induction generators for decentralized energy production, complemented by an energy storage system using Li-Ion batteries. The proposed control strategies employing proportional-integral (PI) controllers effectively manage energy production in both grid-connected and standalone modes. The integration of the Li-Ion battery energy storage system enhances system reliability by mitigating production deficits and storing excess energy. MATLAB/Simulink simulations underscored efficient coordination among production sources, the grid, and local loads.

The next challenge identified in this study is to develop a control strategy that integrates reactive power compensation to limit reactive power injection into the grid, particularly during disturbances associated with adding loads to the LCL filter. Subsequently, a unified control strategy encompassing both grid-connected and autonomous modes will be explored, incorporating an energy management algorithm.

Author Contributions: Conceptualization, M.O., A.Y. and F.B.; Methodology, M.O., A.Y. and F.B.; Software, M.O., A.Y. and F.B.; Validation, M.O., A.Y. and F.B.; Formal analysis, M.O., A.Y. and F.B.; Investigation, M.O., A.Y. and F.B.; Resources, M.O., A.Y. and F.B.; Data curation, M.O., A.Y. and F.B.; Writing—original draft, M.O., A.Y. and F.B.; Writing—review & editing, M.O., A.Y. and F.B.; Visualization, M.O., A.Y. and F.B.; Supervision, M.O., A.Y. and F.B.; Project administration, M.O., A.Y. and F.B.; Funding acquisition, M.O., A.Y. and F.B. All authors have read and agreed to the published version of the manuscript.

Funding: This research was funded by the «Hauts de France» Region Council and Grand-Soissons Agglomeration.

Data Availability Statement: No new data were created or analyzed in this study.

Conflicts of Interest: The authors declare no conflict of interest.

Appendix A

SC6PIG	Squirrel Cage Six-Phase Induction Generator
BDC	Bidirectional DC-DC converter
PLL	Phase locked loop
DG	Distributed generator
IGBT	Isolate gate bipolar transistor
FOC	Field-oriented control
VSI	Voltage source inverter
THD	Total harmonic distortion
PI	Proportional integral
FLC	Fuzzy logic controller

Appendix B

Table A1. Rated parameters of the SC6PIG.

Parameter	Value	Unit
Rated Power	24	Kw
Rated Torque	2350	Nm
Rated Voltage	230	V
Rated Speed	119	Rpm
Rated Current	32.3	A
Frequency	25	Hz
Number of pole pairs	12	-
Stator Resistance R_s	0.262	Ω
Rotor Resistance R_r	0.64	Ω
Stator Inductance L_s	0.0827	H
Rotor Inductance L_r	0.0813	H
Mutual Inductance M	0.0789	H
Friction Coefficient	21.39	Nm/rad/s
Inertia Coefficient	704	Kg·m ²

Table A2. Rated parameters of the battery (Li-Ion).

Parameter	Value	Unit
Total energy capacity	9.8 kWh@25 °C (77 °F), 100% SOC	-
Battery capacity	63	Ah
Voltage range	Charge (468 to 550 Vdc)	V
	Discharge (430 to 507 Vdc)	V
Current range	Charge (10.7 A@467 V)	A
	Discharge (11.7 A@427 V)	A

Table A3. Rated parameters of the grid's side components.

Parameter	Value	Unit
DC bus voltage	650	V
Filter resistors (R_1 & R_2)	0.2	Ω
Filter inductance (L_1 & L_2)	1500 & 750	μ H

Table A3. *Cont.*

Parameter	Value	Unit
Filter capacitors	10	μf
Grid voltage	400	V
Frequency	50	Hz

Appendix C

Table A4. PIC parameters in FOC.

Parameters	Value
Proportional gain K_i	1383
Proportional gain k_p	5.5

Table A5. PIC parameters in grid-connected system.

Parameters	Value
Proportional gain K_i (I_{dq})	100
Proportional gain k_p (I_{dq})	2.5
Proportional gain K_i (V_{dc})	5
Proportional gain k_p (V_{dc})	0.5
Proportional gain K_i (I_{bat})	25
Proportional gain k_p (I_{bat})	0.001

Table A6. PIC parameters in standalone system.

Parameters	Value
Proportional gain K_i (I_{dq})	100
Proportional gain k_p (I_{dq})	0.001
Proportional gain K_i (V_{dq})	0.1
Proportional gain k_p (V_{dq})	10
Proportional gain K_i (V_{dc})	100
Proportional gain k_p (V_{dc})	0.01
Proportional gain K_i (I_{bat})	25
Proportional gain k_p (I_{bat})	0.01

References

- Li, L.; Lin, J.; Wu, N.; Xie, S.; Meng, C.; Zheng, Y.; Wang, X.; Zhao, Y. Review and outlook on the international renewable energy development. *Energy Built Environ.* **2022**, *3*, 139–157. [CrossRef]
- Hoq, M.T.; Nawshad, U.; Islam, M.; Sina, I.; Syfullah, M.; Rahman, R. Micro Hydro Power: Promising Solution for Off-Grid Renewable Energy Source. *Int. J. Sci. Eng. Res.* **2011**, *2*, 1–5.
- Nababan, S.; Muljadi, E.; Blaabjerg, F. An overview of power topologies for micro-hydro turbines. In Proceedings of the 2012 3rd IEEE International Symposium on Power Electronics for Distributed Generation Systems (PEDG), Aalborg, Denmark, 25–28 June 2012; IEEE: Piscataway, NJ, USA, 2012; pp. 737–744. [CrossRef]
- Worku, M. Recent Advances in Energy Storage Systems for Renewable Source Grid Integration: A Comprehensive Review. *Sustainability* **2022**, *14*, 5985. [CrossRef]
- Micro Hydro Power (MHP)-Pros and Cons-Energypedia. Available online: [https://energypedia.info/wiki/Micro_Hydro_Power_\(MHP\)_-_Pros_and_Cons](https://energypedia.info/wiki/Micro_Hydro_Power_(MHP)_-_Pros_and_Cons) (accessed on 11 January 2024).
- Youssef, K.H.; Wahba, M.A.; Yousef, H.A.; Omar, A.S. A new method for voltage and frequency control of stand-alone self-excited induction generator using PWM converter with variable DC link voltage. In Proceedings of the 2008 American Control Conference, Seattle, WA, USA, 11–13 June 2008; IEEE: Piscataway, NJ, USA, 2008; pp. 2486–2491. [CrossRef]
- Didik, H.; Bambang, P.N.; Asep, S.; Purwanto, Y.A. Sustainability Challenge of Micro Hydro Power Development in Indonesia. *IOP Conf. Ser. Earth Environ. Sci.* **2018**, *147*, 012031. [CrossRef]
- Using Regulated Electrical Machines in Small Hydropower Plants Operating in a Power Network | Russian Electrical Engineering. Available online: <https://link.springer.com/article/10.3103/S1068371218050061> (accessed on 11 January 2024).

9. Pantea, A.; Yazidi, A.; Betin, F.; Capolino, G.A.; Lanfranchi, V. Six-phase Axial Flux Permanent Magnet generator model: Simulation and experimental validation. In Proceedings of the 2016 IEEE 25th International Symposium on Industrial Electronics (ISIE), Santa Clara, CA, USA, 8–10 June 2016; IEEE: Piscataway, NJ, USA, 2016; pp. 192–197. [CrossRef]
10. Semail, E.; Meibody-Tabar, F.; Benkhoris, M.F.; Razik, H.; Pietrzak-David, M.; Monmasson, E.; Bouscayrol, A.; Davat, B.; Delarue, P.; Fornel, B.; et al. Machines polyphasées: De la modélisation multimachine à la commande. *J3ea* **2005**, *4*, 12. [CrossRef]
11. Abdel-Khalik, A.S.; Ahmed, S. Performance Evaluation of a Five-Phase Modular Winding Induction Machine. *IEEE Trans. Ind. Electron.* **2012**, *59*, 2654–2669. [CrossRef]
12. Kulandaivel, G.; Sundaram, E.; Gunasekaran, M.; Chenniappan, S. Five-phase induction motor drive-A comprehensive review. *Front. Energy Res.* **2023**, *11*, 1178169. [CrossRef]
13. Yazidi, A.; Pantea, A.; Betin, F.; Carriere, S.; Henao, H.; Capolino, G.-A. Six-phase induction machine model for simulation and control purposes. In Proceedings of the IECON 2014—40th Annual Conference of the IEEE Industrial Electronics Society, Dallas, TX, USA, 29 October 2014–1 November 2014; IEEE: Piscataway, NJ, USA, 2014; pp. 881–887. [CrossRef]
14. Pantea, A.; Yazidi, A.; Betin, F.; Taherzadeh, M.; Carriere, S.; Henao, H.; Capolino, G.-A. Six-Phase Induction Machine Model for Electrical Fault Simulation Using the Circuit-Oriented Method. *IEEE Trans. Ind. Electron.* **2016**, *63*, 494–503. [CrossRef]
15. Chandramohan, K.; Kalyanasundaram, R. Dynamic Modeling of Seven-Phase Induction Generator. *Energy Procedia* **2017**, *117*, 369–376. [CrossRef]
16. De Souza, T.S.; Bastos, R.R.; Cardoso Filho, B.J. Modeling and Control of a Nine-Phase Induction Machine with Open Phases. *IEEE Trans. Ind. Appl.* **2018**, *54*, 6576–6585. [CrossRef]
17. Masoud, M.I.; Abdelkhalik, A.S. Performance Evaluation of Eleven-Phase Induction Machine with Different PWM Techniques. *J. Eng. Res. TJER* **2015**, *12*, 1–14. [CrossRef]
18. Pantea, A. Modélisation, Simulation et Contrôle D'une Génératrice Multiphasée à Grand Nombre de Pôles Pour L'éolien. Available online: <https://theses.hal.science/tel-03650568> (accessed on 23 June 2024).
19. Pantea, A.; Yazidi, A.; Betin, F.; Carriere, S.; Capolino, G.-A. Simulation and experimental control of six-phase induction generator for wind turbines. In Proceedings of the 2016 XXII International Conference on Electrical Machines (ICEM), Lausanne, Switzerland, 4–7 September 2016; IEEE: Piscataway, NJ, USA, 2016; pp. 1181–1186. [CrossRef]
20. Alattar, M.; Alsammak, A. Speed Control of Asymmetrical Six Phase Induction Motor based Fuzzy Logic Controller. *Int. Res. J. Eng. Technol. IRJET* **2020**, *7*, 213–217.
21. Pantea, A.; Yazidi, A.; Betin, F.; Carriere, S.; Sivert, A.; Capolino, G.-A. Fault tolerant control of six-phase induction generator for wind turbines. In Proceedings of the 2017 IEEE International Electric Machines and Drives Conference (IEMDC), Miami, FL, USA, 21–24 May 2017; IEEE: Piscataway, NJ, USA, 2017; pp. 1–7. [CrossRef]
22. Abdel-Khalik, A.S.; Abdel-Majeed, M.S.; Ahmed, S. Effect of Winding Configuration on Six-Phase Induction Machine Parameters and Performance. *IEEE Access* **2020**, *8*, 223009–223020. [CrossRef]
23. Pantea, A.; Yazidi, A.; Betin, F.; Carriere, S.; Sivert, A.; Vacossin, B.; Henao, H.; Capolino, G.-A. Fault-Tolerant Control of a Low-Speed Six-Phase Induction Generator for Wind Turbines. *IEEE Trans. Ind. Appl.* **2019**, *55*, 426–436. [CrossRef]
24. Pantea, A.; Yazidi, A.; Betin, F.; Carriere, S.; Sivert, A.; Capolino, G.-A. Fault Tolerant Control of Six-Phase Induction Gene.Pdf. 2017. Available online: <https://ieeexplore.ieee.org/stampPDF/getPDF.jsp?tp=&a-number=8002161&ref=aHR0cHM6Ly9pZWVleHBsb3JlLmlLZWUub3JnL2Fic3RyYWN0L2RvY3VtZW50LzgwMDIxNjE=> (accessed on 22 January 2024).
25. Pantea, A.; Nurwati, T.; Yazidi, A.; Betin, F.; Carriere, S.; Capolino, G.-A. Fuzzy Logic Control of a Low Speed Six-Phase Induction Generator for Wind Turbines. In Proceedings of the IECON 2018-44th Annual Conference of the IEEE Industrial Electronics Society, Washington, DC, USA, 21–23 October 2018; IEEE: Piscataway, NJ, USA, 2018; pp. 5813–5818. [CrossRef]
26. OBouyahia, O.; Yazidi, A.; Betin, F.; Capolino, G.-A. Fuzzy Variable Structure Control of a Six Phase Induction Generator. In Proceedings of the 2023 IEEE International Electric Machines & Drives Conference (IEMDC), San Francisco, CA, USA, 15–18 May 2023; IEEE: Piscataway, NJ, USA, 2023; pp. 1–6. [CrossRef]
27. Bouyahia, O.; Betin, F.; Yazidi, A. Fault-tolerant Variable Structure Control of a Low Speed 6-Phase Induction Generator. In Proceedings of the 2021 IEEE 13th International Symposium on Diagnostics for Electrical Machines, Power Electronics and Drives (SDEMPED), Dallas, TX, USA, 22–25 August 2021; IEEE: Piscataway, NJ, USA, 2021; pp. 92–98. [CrossRef]
28. Raza, A.; Xu, D.; Mian, M.; Ahmed, J. A micro hydro power plant for distributed generation using municipal water waste with archimedes screw. In Proceedings of the 2013 16th International Multi Topic Conference, INMIC 2013, Lahore, Pakistan, 19–20 December 2013; pp. 66–71. [CrossRef]
29. Analysis and Controller Design for Stand-Alone VSIs in Synchronous Reference Frame-Ramezani-2017-IET Power Electronics-Wiley Online Library. Available online: <https://ietresearch.onlinelibrary.wiley.com/doi/10.1049/iet-pel.2016.0883> (accessed on 27 January 2024).
30. Ünlü, M.; Çamur, S.; Beşer, E.; AriFoğlu, B. Sinusoidal current injection based on a line-commutated inverter for single-phase grid-connected renewable energy sources. *Turk. J. Elec. Eng. Comp. Sci.* **2016**, *24*, 4670–4681. [CrossRef]
31. Liu, Z.; Liu, J.; Zhao, Y. A Unified Control Strategy for Three-Phase Inverter in Distributed Generation. *IEEE Trans. Power Electron.* **2014**, *29*, 1176–1191. [CrossRef]
32. Sedo, J.; Kascak, S. Design of output LCL filter and control of single-phase inverter for grid-connected system. *Electr. Eng.* **2017**, *99*, 1217–1232. [CrossRef]

33. Jo, J.; Liu, Z.; Cha, H. A New Design Method of LCL Filter for Single Phase Grid Connected Power Converter. In Proceedings of the 2019 International Symposium on Electrical and Electronics Engineering (ISEE), Ho Chi Minh, Vietnam, 10–12 October 2019; IEEE: Piscataway, NJ, USA, 2019; pp. 189–193. [[CrossRef](#)]
34. Liserre, M.; Blaabjerg, F.; Hansen, S. Design and Control of an LCL-Filter-Based Three-Phase Active Rectifier. *IEEE Trans. Ind. Applicat.* **2005**, *41*, 1281–1291. [[CrossRef](#)]
35. Dhaneria, A.; Khambhadiya, H. Design of AC side filter for Grid Tied Solar Inverter. In Proceedings of the 2019 4th International Conference on Recent Trends on Electronics, Information, Communication & Technology (RTEICT), Bangalore, India, 17–18 May 2019; IEEE: Piscataway, NJ, USA, 2019; pp. 1375–1378. [[CrossRef](#)]
36. Arab, N.; Kedjar, B.; Al-Haddad, K. D-Q frame optimal control of single phase grid connected inverter with LCL filter. In Proceedings of the 2016 IEEE Electrical Power and Energy Conference (EPEC), Ottawa, ON, Canada, 12–14 October 2016; IEEE: Piscataway, NJ, USA, 2016; pp. 1–6. [[CrossRef](#)]
37. Wu, W.; He, Y.; Tang, T.; Blaabjerg, F. A New Design Method for the Passive Damped LCL and LLCL Filter-Based Single-Phase Grid-Tied Inverter. *IEEE Trans. Ind. Electron.* **2013**, *60*, 4339–4350. [[CrossRef](#)]
38. Chou, S.-F.; Wang, X.; Blaabjerg, F. Passivity-based LCL Filter Design of Grid-Connected VSCs with Converter Side Current Feedback. In Proceedings of the 2018 International Power Electronics Conference (IPEC-Niigata 2018-ECCE Asia), Niigata, Japan, 20–24 May 2018; IEEE: Piscataway, NJ, USA, 2018; pp. 1711–1718. [[CrossRef](#)]
39. Wang, X.; Blaabjerg, F.; Loh, P.C. Passivity-Based Stability Analysis and Damping Injection for Multiparalleled VSCs with LCL Filters. *IEEE Trans. Power Electron.* **2017**, *32*, 8922–8935. [[CrossRef](#)]
40. Chinmaya, K.A.; Singh, G.K. Modeling and experimental analysis of grid-connected six-phase induction generator for variable speed wind energy conversion system. *Electr. Power Syst. Res.* **2019**, *166*, 151–162. [[CrossRef](#)]
41. Singh, G.K. Modeling and experimental analysis of a self-excited six-phase induction generator for stand-alone renewable energy generation. *Renew. Energy* **2008**, *33*, 1605–1621. [[CrossRef](#)]
42. Nurwati, T. Contribution to Fuzzy Logic Controller of Six-Phase Induction Generator for Wind Turbine Application. Ph.D. Thesis, University of Picardie Jules Verne, Amiens, France, 2019. Available online: <https://www.theses.fr/2019AMIE0064> (accessed on 23 January 2024).
43. Aroquiadassou, G.; Henao, H.; Capolino, G.A.; Boglietti, A.; Cavagnino, A. A simple circuit-oriented model for predicting six-phase induction machine performances. In Proceedings of the IECON 2006-32nd Annual Conference on IEEE Industrial Electronics, Paris, France, 6–10 November 2006; IEEE: Piscataway, NJ, USA, 2006; pp. 1441–1446. [[CrossRef](#)]
44. Renukadevi, G.; Rajambal, K. Generalized model of multi-phase induction motor drive using matlab/simulink. In *ISGT2011-India*; IEEE: Piscataway, NJ, USA, 2011; pp. 114–119. [[CrossRef](#)]
45. Baghli, L. Modélisation et Commande de la Machine Asynchrone. 2020. Available online: https://www.baghli.com/dl/courscmd/cours_cmde_MAS.pdf (accessed on 28 January 2024).
46. Bouyahia, O. Génération Électrique Tolérante Aux Défauts à Base de Structures Multiphasées: Comparaison, Choix D'une Technologie, Transfert Technologique. Ph.D. Thesis, Université de Picardie Jules Verne, Amiens, France, 2022. Available online: <https://theses.hal.science/tel-04073881> (accessed on 28 January 2024).
47. Abdulelah, A.M.; Ouahid, B.; Youcef, S. Control of a Stand-Alone Variable Speed Wind Turbine with a Permanent Magnet Synchronous Generator. In Proceedings of the 2021 18th International Multi-Conference on Systems, Signals & Devices (SSD), Monastir, Tunisia, 22–25 March 2021; pp. 546–550. [[CrossRef](#)]
48. Bourguiba, I.; Houari, A.; Belloumi, H.; Kourda, F. Control of single-phase grid connected photovoltaic inverter. In Proceedings of the 2016 4th International Conference on Control Engineering & Information Technology (CEIT), Hammamet, Tunisia, 16–18 December 2016; IEEE: Piscataway, NJ, USA, 2016; pp. 1–6. [[CrossRef](#)]
49. Das Gupta, T.; Kumar, D.; Chaudhary, K. Modelling and analysis of grid-tied fuel cell system with synchronous reference frame control. In Proceedings of the 2017 4th International Conference on Power, Control & Embedded Systems (ICPCES), Allahabad, India, 9–11 March 2017; IEEE: Piscataway, NJ, USA, 2017; pp. 1–6. [[CrossRef](#)]
50. Wang, C.; Sun, J. Study on control method for the grid-connected inverter with LCL filter. In Proceedings of the 2014 IEEE Workshop on Advanced Research and Technology in Industry Applications (WARTIA), Ottawa, ON, Canada, 29–30 September 2014; IEEE: Piscataway, NJ, USA, 2014; pp. 1337–1341. [[CrossRef](#)]
51. Hamrouni, N.; Jraidi, M.; Chérif, A. New method of current control for LCL-interfaced grid-connected three phase voltage source inverter. *Rev. Des Energ. Renouvelables* **2010**, *13*, 71. [[CrossRef](#)]
52. Sagiraju, D.; Obulesu, Y.P.; Choppavarapu, S. Dynamic performance improvement of standalone battery integrated PMSG wind energy system using proportional resonant controller. *Eng. Sci. Technol. Int. J.* **2017**, *20*, 1353–1365. [[CrossRef](#)]
53. Sahu, P.K.; Jena, S.; Babu, B.C. Power management and bus voltage control of a battery backup-based stand-alone PV system. *Electr. Eng.* **2022**, *104*, 97–110. [[CrossRef](#)]
54. Bidirectional DC-DC Converter in Solar PV System for Battery Charging Application | IEEE Conference Publication | IEEE Xplore. Available online: <https://ieeexplore.ieee.org/document/8537391> (accessed on 24 January 2024).

55. Wang, Y.-X.; Qin, F.-F.; Kim, Y.-B. Bidirectional DC-DC converter design and implementation for lithium-ion battery application. In Proceedings of the 2014 IEEE PES Asia-Pacific Power and Energy Engineering Conference (APPEEC), Hong Kong, China, 7–10 December 2014; pp. 1–5. [[CrossRef](#)]
56. Hussein, M.M.; Senjyu, T.; Orabi, M.; Wahab, M.A.A.; Hamada, M.M. Control of a Stand-Alone Variable Speed Wind Energy Supply System. *Appl. Sci.* **2013**, *3*, 437–456. [[CrossRef](#)]

Disclaimer/Publisher’s Note: The statements, opinions and data contained in all publications are solely those of the individual author(s) and contributor(s) and not of MDPI and/or the editor(s). MDPI and/or the editor(s) disclaim responsibility for any injury to people or property resulting from any ideas, methods, instructions or products referred to in the content.